ACS APPLIED MATERIALS & INTERFACES

Research Article

www.acsami.org

Bimodal Sintered Silver Nanoparticle Paste with Ultrahigh Thermal Conductivity and Shear Strength for High Temperature Thermal Interface Material Applications

Mingyu Li,* Yong Xiao, Zhihao Zhang,* and Jie Yu

State Key Laboratory of Advanced Welding and Joining, Harbin Institute of Technology Shenzhen Graduate School, Shenzhen 518055, People's Republic of China

Supporting Information

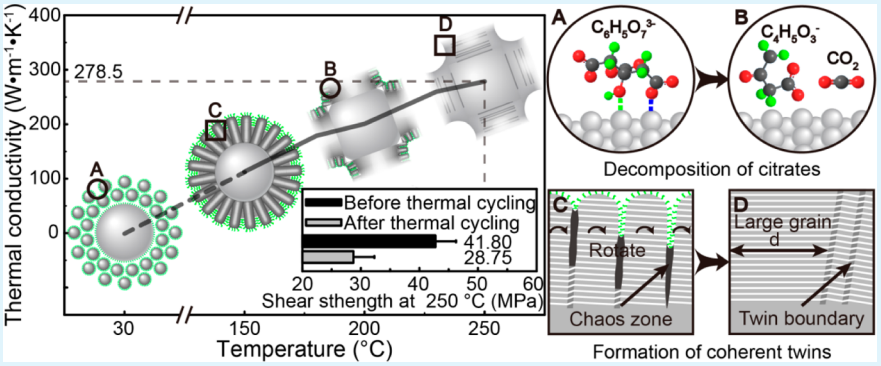

ABSTRACT: A bimodal silver nanoparticle (AgNP) paste has been synthesized via the simple ultrasonic mixing of two types of unimodal AgNPs (10 and 50 nm in diameter). By sintering this paste at 250 °C for 30 min, we obtained an ultrahigh thermal conductivity of 278.5 W m^{-1} K^{-1}, approximately 65% of the theoretical value for bulk Ag. The shear strength before and after thermal cycling at 50−200 °C for 1000 cycles was approximately 41.80 and 28.75 MPa, respectively. The results show that this excellent performance is attributable to the unique sintered structures inside the bimodal AgNP paste, including its low but stable porosity and the high density coherent twins. In addition, we systematically discuss the sintering behavior of this paste, including the decomposition of the organic layers and the formation of the coherent twins. On the basis of these results, we confirm that our bimodal AgNP paste has excellent potential as a thermal interface material for high temperature power device applications.

KEYWORDS: *silver nanoparticles, bimodal size distribution, sintering, thermal interface material, thermal conductivity, twin formation*

INTRODUCTION

Due to their unique size-dependent properties, silver nanoparticles (AgNPs) have attracted immense scientific and technological interest from a broad range of fields, such as catalysis, optics, and biomedicine.[1−5] These applications cannot tolerate the uncontrolled agglomeration of AgNPs because the aggregated particles will easily lose their size effect and their properties will rapidly revert to those of the bulk material.[6,7] Interestingly, for thermal interface material (TIM) applications, this agglomeration behavior promotes short-duration and low temperature interconnection, and the resultant structure exhibits the excellent characteristics of the bulk Ag, such as high thermal and electric conductivities, good shear strength, and high temperature operating capability (over 300 °C).[8−11] More importantly, traditional TIMs (i.e., Sn-based solder alloys and other conductive adhesives[12,13]) cannot satisfy the extreme requirements of high temperature power device applications, whose utilization temperatures may exceed 250 °C, while the novel developed TIMs (i.e., grapheme and multilayer grapheme nanocomposites[14,15]) lack sufficient thermal conductivity to facilitate power device cooling. Therefore, AgNPs will undoubtedly open new avenues for the development of high temperature TIMs in the field of advanced microelectronics.

Because the synthesis routes of AgNPs of various sizes have gradually matured over the past decade,[1,16−18] the research focus regarding sintered AgNPs has shifted from realizing short-duration and low temperature interconnections to improving the performance of sintered structures.[10,12,19] Thermal conductivity (TC) is certainly one of the most important indicators for TIM applications, as it can directly determine the heat removal capability of the power devices.[15] However, few studies in the literature have achieved even half of the theoretical value of the bulk Ag (429 W m^{-1} K^{-1}). Yu et al.[12] studied the thermal resistances of sintered AgNPs with a size distribution of 20−120 nm at 100−250 °C. In their study, ultralow thermal resistances of less than 2 mm K W^{-1} were obtained at the optimum particle size of 20−30 nm at 250 °C. Interestingly, numerous ∼50 nm sintered voids were found in

Received: February 10, 2015
Accepted: April 20, 2015
Published: April 20, 2015

DOI: 10.1021/acsami.5b01341
ACS Appl. Mater. Interfaces 2015, 7, 9157−9168

their structures, and the effect of these voids on the TC merits further consideration. Moreover, Wang et al.[20] found that the sintering density of the sintered AgNPs could be further increased by using smaller AgNPs (with a mean diameter of 13 nm) and thinner organic protecting shells on the particle surfaces; they reported a maximum TC of 229 W m^{-1} K^{-1}, the highest value ever observed. Unfortunately, numerous crystallographic defects (e.g., large-angle grain boundaries) were found inside their sintered structures, which might have exerted an enormous negative effect on the final thermal performance. The lack of a means to increase the density of the sintered structure while minimizing the intrinsic defects prevents the utilization of AgNPs in a wide range of TIM applications.

The service reliability of the sintered AgNPs is another essential indicator for TIM applications.[21,22] When the power device is switched at high frequency, the accumulated temperature is especially prone to breaking at 150 °C and causes the sintered AgNPs to continuously shrink during usage.[23,24] Conversely, the semiconductor chip and heat-sinking substrate connected by the sintered AgNPs will concurrently expand as the temperature increases, generating severe thermo-mechanical stress, which may result in serious reliability issues for the sintered joints.[22,25] More importantly, due to the significant differences in the coefficients of thermal expansion (CTEs) between the chip and substrate, the failure risk of the AgNPs' interconnected layers may be further aggravated when the ambient temperature is changed. Although some additives in AgNP pastes (e.g., diamond[26] and silicon carbide particles[27]) have proven effective in reducing the shrinkage of the sintered structures during usage, a reduction in the corresponding thermal performance caused by these heterogeneous particles seems unavoidable. Therefore, identifying sintered AgNPs with suitable CTE values to maintain sufficient chip-attachment strength (shear strength) after high temperature power cycling remains a technical challenge.

Regardless of whether a single species of AgNPs with a unimodal size distribution is used or dopants are added, the performance of the sintered AgNPs will be degraded to some extent.[12,28,29] Therefore, an attempt is made to develop a TIM paste containing a bimodal size distribution of AgNPs (Figure 1), in which the small particles are used as the "filler" to increase the initial stacking density and "weld" the particle surfaces together at a relatively low temperature, while the large particles are used as the "framework" to minimize initial crystallographic defects and stabilize the final structure after sintering. In this paper, a bimodal AgNP paste endowed with excellent thermal and mechanical performance during sintering has been synthesized via the simple ultrasonic mixing of two types of unimodal AgNPs. In addition, the corresponding sintering mechanisms, including the decomposition of the organic protecting layer and the structural evolution of AgNPs, are also discussed systematically.

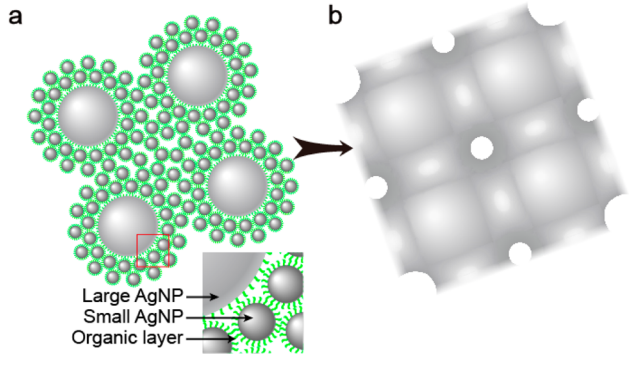

Figure 1. Hypothetical schematic representation of AgNPs-BM (a) before sintering and (b) after sintering.

EXPERIMENTAL SECTION

Materials. Silver nitrate ($AgNO_3$), sodium citrate dihydrate (Na_3citrate·$2H_2O$), iron sulfate heptahydrate ($FeSO_4·7H_2O$), and sodium nitrate ($NaNO_3$) were supplied by Sigma-Aldrich. All of these reagents were used as received. Deionized water (Millipore Milli-Q grade) with a resistivity of 18.2 MΩ cm^{-1} was used in the experiments, and all glassware was cleaned in a bath of aqua regia solution before use. In addition, Si chips (1.5 × 1.5 × 0.75 mm^3), metalized with TiW (0.2 μm)/Cu(20 μm) films on the back, were supplied by MTI Corporation, and Cu (20 μm) metalized ceramic substrates, purchased from Kyocera, were selected as the package substrates.

Synthesis of the Small AgNPs. The small AgNPs were synthesized on the basis of a modification of Carey Lea's method.[30] Briefly, a mixed reducing agent of 35 mL of Na_3citrate·$2H_2O$ solution (400 g L^{-1}) and 25 mL of $FeSO_4·7H_2O$ solution (300 g L^{-1}) was added to 25 mL of $AgNO_3$ solution (100 g L^{-1}). When the blue-black precipitate was completely flocculated, the supernatant was discarded, and the small AgNPs were obtained by condensing the precipitate after centrifuging at 3500 rpm for 5 min.

Synthesis of the Large AgNPs. The large AgNPs were prepared as described by Lee and Meisel.[31] Specifically, 500 mL of $AgNO_3$ solution (0.54 g L^{-1}) was boiled with continuous stirring. Subsequently, 30 mL of Na_3citrate solution (10 g L^{-1}) was added, and the mixture was further boiled for 1 h. After the solution had cooled to 20 °C, the cyan supernatant was precipitated with 5 mL of Na_3citrate·$2H_2O$ solution (400 g L^{-1}). Finally, the large AgNPs were obtained by condensing these precipitates by centrifugation at 3500 rpm for 5 min.

Optimization of the Weight Ratio for the Bimodal AgNP Paste. We assumed that one large AgNP would be closely surrounded by a layer of the small AgNPs to form a unit sphere, and the ideal entity of the bimodal AgNP paste should be composed of cubic unit cells with the unit spheres located at the corners and the centers of all the cube faces (see Supporting Information Figure S1). On the basis of the calculation, the weight ratio of the small and large AgNPs should be nearly 2:1, and the theoretical limit of the porosity for the bimodal AgNP paste should be 21.9%.

Preparation of the Bimodal AgNP Paste. The as-prepared small and large AgNPs in a certain weight ratio (2:1) were dispersed in the deionized water under supersonic stirring for 30 min, flocculated with $NaNO_3$ solution (85 g L^{-1}), and then centrifuged at 3500 rpm for 5 min. According to the previous study, the organic protecting shells, which were composed of citrates on Ag surfaces, prevent the self-cohesion of AgNPs but can also reduce the surface activation of AgNPs.[6,32] To remove these organic shells appropriately, after centrifuging, the resulting precipitates were redispersed in deionized water, flocculated with $NaNO_3$ solution, and centrifuged using the same experimental parameters. After this process was repeated twice, the bimodal AgNP paste was obtained.

Preparation of the Sintered Structures Using the Bimodal AgNP Paste. The as-prepared bimodal AgNP paste was divided into two samples. One was directly heated in an oven (FD23, Binder) up to 150, 200, or 250 °C at a heating rate of 5 °C min^{-1} in air atmosphere, followed by an isothermal hold for 30 min. The resultant sintered structures were collected and sorted for subsequent tests. The other sample was coated on Si chips and stacked on the ceramic substrates to form sandwiched samples with the bimodal AgNP paste in the middle. Subsequently, the sandwiched samples were also heated using the same experimental conditions and prepared for subsequent tests.

Instruments and Measurements. Transmission electron microscope (TEM) images were obtained with a FEI Tecnai G2T20 electron microscope operated at 200 kV. Scanning electron

DOI: 10.1021/acsami.5b01341
ACS Appl. Mater. Interfaces 2015, 7, 9157–9168

microscopy (SEM) images were obtained using a Hitachi S4800 apparatus. Differential scanning calorimetry (DSC) and thermogravimetric analysis (TGA) were synchronously performed using a Netzsch STA-449 thermogravity analyzer in an air atmosphere, and the preset temperature profile consisted of three stages: heating (5 °C min^{-1}) from 25 to 120 °C, holding at 120 °C for 20 min, and heating (1 °C min^{-1}) from 120 to 260 °C. Thermal conductivity (k) data were obtained from the equation $k = \alpha\rho c$, where α is the thermal diffusion coefficient measured using a laser flash apparatus (Netzsch, LFA457), ρ is the density, and c is the specific heat capacity obtained by DSC using a sapphire sample as a reference. The porosities of the sintered structures were measured using the Archimedes method. The crystalline sizes of the sintered structures were estimated from the full-width at half-maximum intensity values of the X-ray diffraction (XRD, Rigaku, D/max-2500PC, Cu Kα) peaks using the Scherrer method (for more details, see Supporting Information Figure S2). CTE measurements were performed using a thermo-mechanical analyzer (Shimadzu, TMA-60) under air atmosphere from 30 to 600 °C at a heating rate of 5 °C min^{-1}. Thermal cycle tests were conducted in a thermal shock chamber (ETAC, NT530A) from 50 to 200 °C. Each cycle had a period of 30 min with a hold time of 10 min at both the maximum and minimum temperatures, and the test was conducted for 1000 cycles. The shear strengths before and after thermal cycling were measured at room temperature with a bond tester (Rhesca, PTR-1101); the shear height of the blade tip above the ceramic substrate was 50 μm, and the shear speed was 200 μ s^{-1}.

RESULTS AND DISCUSSION

Sintered Characterization of AgNPs-BM. Figure 2 shows the morphologies of the as-prepared small and large AgNPs;

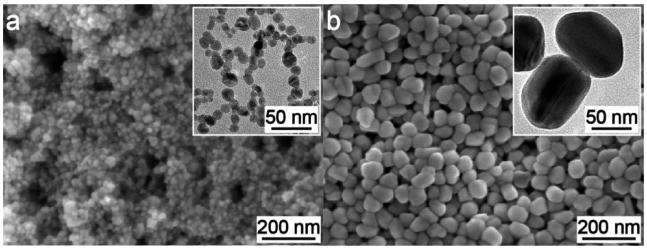

Figure 2. SEM and corresponding TEM images of the as-prepared (a) AgNPs-10 and (b) AgNPs-50 at 30 °C.

the enlarged TEM images are presented as insets in the corresponding SEM images. It can be clearly seen that both small and large AgNPs are uniform in size, with no uncontrolled agglomeration. These particles have average diameters of 10 and 50 nm and are hereafter referred to as AgNPs-10 and AgNPs-50, respectively. As observed in the inset TEM images, the AgNPs-10 are nearly globose with organic layers of 0.5−1 nm thickness on their surfaces, while the AgNPs-50 possess irregular spherical shapes with organic layers of less than 0.3 nm thickness (for more detail, see Supporting Information Figure S3). The difference in the thickness of the organic protecting layers may be related to the encapsulated density of citrates, as discussed below.

Figure 3a shows the morphology of the as-prepared bimodal AgNPs and clearly demonstrates that the AgNPs-10 are perfectly clustered around each AgNP-50. Because no uncontrolled agglomeration occurred between the adjacent AgNPs, we believe that this bimodal AgNP paste was prepared successfully (hereafter, the bimodal AgNPs will be referred to as AgNPs-BM).

Figure 3b−d shows the morphology evolution of AgNPs-BM after sintering at 150−250 °C for 30 min. At 150 °C (Figure

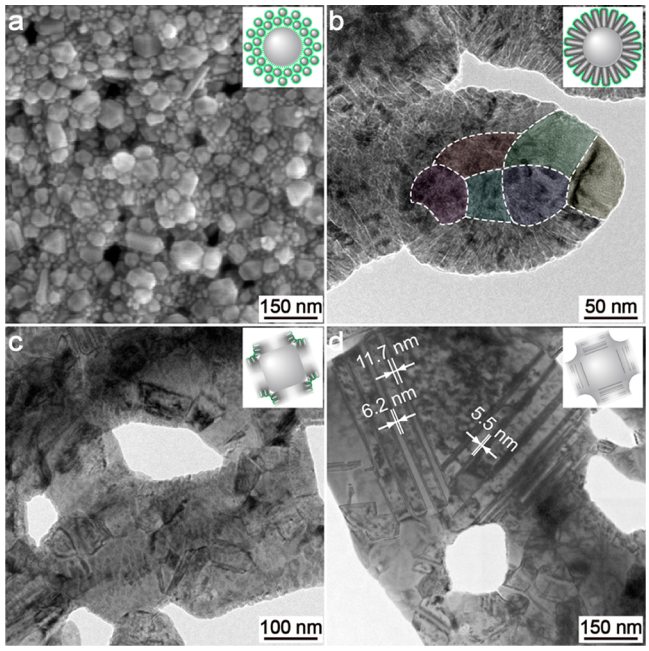

Figure 3. Sintering morphologies of AgNPs-BM at (a) 30 °C, (b) 150 °C (the large grains are delineated by white dashed lines), (c) 200 °C, and (d) 250 °C for 30 min. Some structural schematic diagrams based on the actual sintered structures are also presented as insets in these SEM images.

3b), the AgNPs-BM gradually cluster into sintered islands (200−300 nm in diameter), and the adjacent islands are necked through ray-like grains. Moreover, each sintered island is composed of a few large grains (50−80 nm in diameter) and many small ray-like grains (40−80 nm in height and 5−10 nm in width). The large grain is always located at the center and is covered by a monolayer of the ray-like grains. Undoubtedly, the large grains and the ray-like grains should be formed by the further growth of AgNPs-50 and AgNPs-10, respectively; however, the mechanism underlying this formation remains unclear. In addition, we observe numerous organic layers and amorphous Ag structures mixed inside of the sintered islands, which indicates that the sintering process is only just beginning.

At 200 °C (Figure 3c), the original sintered islands are replaced by some loose sintered frames, which have intertwined to create a three-dimensional network. The number of crystallographic defects in these frames (i.e., the organic and amorphous phases) is obviously decreased relative to that in Figure 3b, and the microstructure of the frames is mainly composed of polygon-like grains in the range 40−100 nm. Interestingly, the monolayer of the ray-like grains can still be seen wrapping the surface of the frames despite a decrease of the heights of these rays to less than 40 nm (from 80 nm). In summary, at this temperature, the sintering process remains ongoing.

At 250 °C (Figure 3d), a densely sintered framework has formed, and no ray-like grains survive, even at the edge of the frames. The organic and amorphous phases inside the frames have disappeared altogether, and the microstructure of the frames is composed of huge grains in the range 50−500 nm. Because the sintered holes inside the framework are nearly circular, we believe that the sintering process is complete.[33] It should also be noted that a high density of twins (5−10 nm in

DOI: 10.1021/acsami.5b01341
ACS Appl. Mater. Interfaces 2015, 7, 9157−9168

thickness) is observed in these frames. The reason for their formation and its effects will be discussed subsequently.

Figure 4a shows the porosities of the three types of AgNPs after sintering at 30−250 °C for 30 min. Clearly, both types of

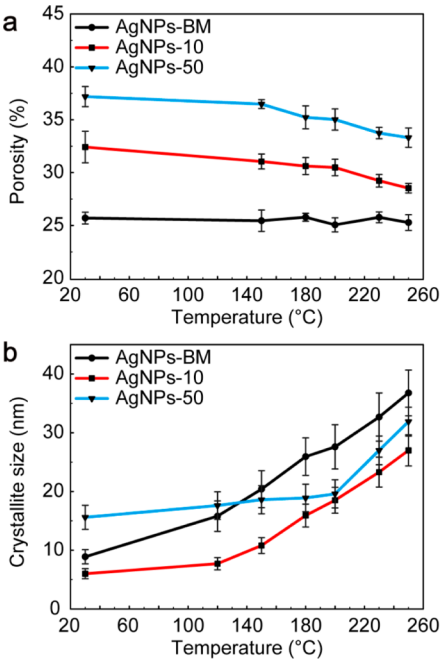

Figure 4. (a) Porosities of the three types of AgNPs after sintering at 30−250 °C for 30 min; the specific values are listed in Supporting Information Table S1. (b) Crystallite sizes of the three types of AgNPs after sintering at 30−250 °C for 30 min; the specific values are listed in Supporting Information Table S2.

unimodal AgNPs have become denser with increasing sintered temperature. As the temperature increases by 220 °C, the porosities of AgNPs-10 (red line) and AgNPs-50 (blue line) decrease by 3.89% and 3.88%, respectively. However, unlike that of unimodal AgNPs, the porosity of AgNPs-BM is stable at nearly 25.5%, and the sintered structure exhibits no obvious shrinkage at any of the selected temperature points (Supporting Information Table S1). More importantly, the porosity curve for AgNPs-BM (black line) is lower than that of any other type of AgNPs at all measured temperatures, indicating that the sintering density has been maximized using AgNPs-BM. It is known that the final density of the sintered structure is mainly determined by the initial stacking density of the AgNPs before sintering.[34] In a unimodal AgNP paste, the interparticle voids are firmly trapped, even in an ideal close-packed structure. However, in a bimodal AgNP paste, the interparticle voids among the large particles can be further filled by small particles. Accordingly, the initial stacking density of the AgNPs can be improved by using AgNPs-BM, consistent with our porosity results. The only unexpected observation is that the structure sintered with AgNPs-BM does not decrease in volume with increasing temperature. Although the reason for this phenomenon remains unclear, it is beneficial for the structural stability of the chip interconnections.

Figure 4b shows the crystallite sizes (CSs) of the three types of AgNPs after sintering at 30−250 °C for 30 min, as determined via X-ray line broadening measurements. At 30 °C, the CSs for AgNPs-BM, AgNPs-10, and AgNPs-50 are 8.9, 6.0, and 15.6 nm, respectively. However, with increasing temperature, all of these curves show a tendency to slowly increase until 120 °C (AgNPs-50 rise until 200 °C) and then rapidly increase from 120 to 250 °C. Accordingly, the CSs reach 36.8 nm for AgNPs-BM, 27.0 nm for AgNPs-10, and 31.9 nm for AgNPs-50 at 250 °C. It should be noted that the CS curve for AgNPs-BM (black line) exceeds that for any other type of AgNPs (blue and red lines) at temperatures above 130 °C, indicating that the crystallographic defects (i.e., the grain boundaries) in the sintered structure of AgNPs-BM are the lowest among the three types of AgNPs in this temperature range. In addition, for AgNPs-BM, the CSs calculated using XRD data are smaller than those determined from the TEM images at the selected temperatures. For example, the CS calculated using XRD results at 250 °C is 36.8 nm, but when TEM is used, this value is 50−500 nm. This difference may be due to the formation of high density twins in the sintered structure, as these twins (5−10 nm in thickness in Figure 3d) are not included in the CS determination using TEM data.

Sintered Performance of AgNPs-BM. Because the sintered structure with the highest density but lowest intrinsic crystallographic defects has been achieved by AgNPs-BM, as expected, we further evaluated its performances for TIM applications. Figure 5 shows the TCs of the three types of

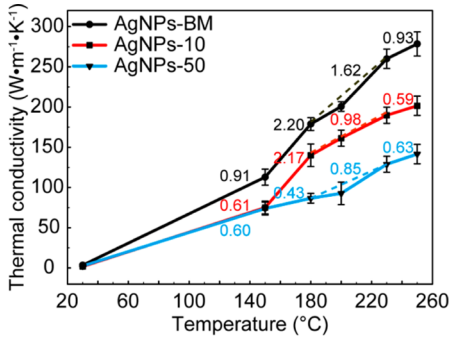

Figure 5. Thermal conductivities of the three types of AgNPs after sintering at 30−250 °C for 30 min; the specific values are listed in Supporting Information Table S3. Note that the value marked in the figure is the slope of the corresponding line segment in W m^{-1} K^{-2}. In addition, the details of the calculation of these thermal conductivity values are presented in the Supporting Information Tables S4−S6.

AgNPs after sintering at 30−250 °C for 30 min. At 30 °C, the initial TCs for AgNPs-BM, AgNPs-10, and AgNPs-50 are 3.3, 1.6, and 2.3 W m^{-1} K^{-1}, respectively, indicating that all of the pastes are poor thermal conductors at this temperature. At 150 °C, the TCs for AgNPs-10 and AgNPs-50 are 75.0 and 73.8 W m^{-1} K^{-1}, respectively, while that for AgNPs-BM is 112.8 W m^{-1} K^{-1}. The value for AgNPs-BM is almost 1.5 times greater than those for the unimodal AgNPs. At 150−180 °C, all of these TC curves exhibit a linear increase (the increase for AgNPs-50 persists until 200 °C) at rates of 2.20 W m^{-1} K^{-2} for AgNPs-BM, 2.17 W m^{-1} K^{-2} for AgNPs-10, and 0.43 W m^{-1} K^{-2} for AgNPs-50. Thus, the TC of AgNPs-BM increases most rapidly, followed by that of AgNPs-10 and then AgNPs-50 in this temperature region. At 180−230 °C, a significant difference in slope among these curves can be clearly observed, with increased rates of 1.62 W m^{-1} K^{-2} for AgNPs-BM, 0.98 W m^{-1} K^{-2} for AgNPs-10, and 0.85 W m^{-1} K^{-2} for AgNPs-50. The value of the TC for AgNPs-BM still increases the most rapidly, reaching 260.7 W m^{-1} K^{-1} at 230 °C. This value is 1.37 times greater than that of AgNPs-10 (189.8 W m^{-1} K^{-1}) and 2.02

DOI: 10.1021/acsami.5b01341
ACS Appl. Mater. Interfaces 2015, 7, 9157−9168

times greater than that of AgNPs-50 (128.9 W m^{-1} K^{-1}). In addition, the increased rates of all TC curves become sluggish at 230−250 °C, and the final value for AgNPs-BM is 278.5 W m^{-1} K^{-1}, which is close to 65% of the theoretical value for bulk Ag.

Clearly, a huge increase in TC has been achieved with AgNPs-BM, but the reason for this increase remains unclear. For a porous material, TC can be expressed as[35−37]

$$k = k_0(1 - \xi)^n \quad (1)$$

where k_0 is the TC of the bulk material, k is the TC of the porous material, ξ is the porosity, and n is the exponent of TC. More precisely, from the microscopic perspective, TC can also be written as[38]

$$k = \frac{a\langle v\rangle \lambda_{bulk} C_v}{3N_A} \quad (2)$$

where a is the number of particles per unit volume, $\langle v\rangle$ is the mean speed, λ_{bulk} is the mean free length of the bulk material, C_v is the molar heat capacity and N_A is Avogadro's number. It should be noted that when the sintered structure is composed of the nanocrystalline material (i.e., the CS of the sintered structure ($d_{sintered}$) is less than λ_{bulk}), the mean free length of the sintered structure ($\lambda_{sintered}$) can be assumed to be equal to the actual value of CS as a first approximation. Hence

$$\frac{k}{k_{sintered}} = \frac{\lambda_{bulk}}{\lambda_{sintered}} \approx \frac{\lambda_{bulk}}{d_{sintered}} \quad (3)$$

Substituting eq 3 into eq 1, we can obtain an equation for the TC of AgNPs-BM.

$$k_{sintered} = \frac{d_{sintered}}{\lambda_{bulk}} k_0(1 - \xi)^n \quad (4)$$

Because k_0 = 429 W m^{-1} K^{-1} and λ_{bulk} = 51 nm,[39] the values of n for AgNPs-BM at 150−250 °C are 0.18−1.43 (Table 1).

Table 1. Values of *n* for AgNPs-BM at 150−250 °C

	150 °C	180 °C	200 °C	230 °C	250 °C
AgNPs-BM	1.43	0.66	0.50	0.18	0.36

Unfortunately, these values seem to be erroneous. Even if the sintered structure is completely composed of one part Ag bulk and one part void, the value of n will be equal to 1 (known as Francl's model[40]). However, in actuality, the value of n is always in the range 1.5−3.[36,37,41] Wang et al.[42] confirmed that the dominant mechanisms for TC reduction in nanocrystalline metals were the effects of porosity and phonon scattering at grain boundaries. However, there are few changes in porosity for AgNPs-BM after sintering at 150−250 °C (black line in Figure 4a). Therefore, if the value of n is calculated to be less than 1, the scattering effects of grain boundaries should be significantly reduced. On the basis of our observation in Figure 3d, high density twins were generated inside the sintered structures for AgNPs-BM. More importantly, the scattering effect of the twin boundary is reported to be 1 order of magnitude lower than that of the conventional high angle grain boundary inside of the bulk metal.[43,44] Because numerous twins are unavoidably counted in the CS analysis of the XRD data, it is reasonable to assume that these twin boundaries inside of the sintered structure should be responsible for the ultrahigh TC of the sintered structure of AgNPs-BM. In addition, according to the variation in the value of n, we believe that the density of the twins inside of the sintered structure may increase from 150 to 230 °C but then slightly decrease after 230 °C.

Figure 6 shows the shear strengths (SSs) of three types of sandwiched AgNP samples after sintering at 150, 200, and 250 °C for 30 min followed by thermal cycling from 50 to 200 °C for 1000 cycles. (Note that the upper temperature limit of the thermal shock chamber (ETAC, NT530A) is limited to 200 °C.) For all samples sintered at 150 °C, slight increases in SS are observed after thermal cycling. For example, the SS of AgNPs-BM was 19.12 MPa after thermal cycling, which is nearly 5 MPa higher than the value before thermal cycling (for more details, see Supporting Information Table S7). This increase may be due to the fact that the sintering process can proceed when the cycling temperature is above 150 °C. Interestingly, for all samples sintered at 200 °C, the increases in SS are sharper than those for the samples sintered at 150 °C before thermal cycling. In particular, the SS for AgNPs-BM was 39.94 MPa. However, sharp drops in SS are detected after thermal cycling, and the values for AgNPs-BM, AgNPs-10, and AgNPs-50 were 46.7%, 44.2%, and 68.1% of the initial values, respectively. Encouragingly, the SS for AgNPs-BM after thermal cycling (18.68 MPa) is higher than those for the unimodal AgNPs, although the differences are not very large. All samples sintered at 250 °C also exhibited similar reductions in the SS after thermal cycling. However, the value for AgNPs-BM (28.75 MPa) does not decrease substantially after thermal cycling. This value is more than twice those obtained for the unimodal AgNPs after thermal cycling and is much higher than those obtained for Sn−Ag or Sn−Ag−Cu solders (8−18.4 MPa) under similar conditions.[45,46] Accordingly, we believe that a satisfactory bonding strength can be achieved with AgNPs-BM after sintering at 250 °C for 30 min.

On the basis of the previous study, the thermal mismatches among Si chips, sintered AgNPs, and ceramic substrates can

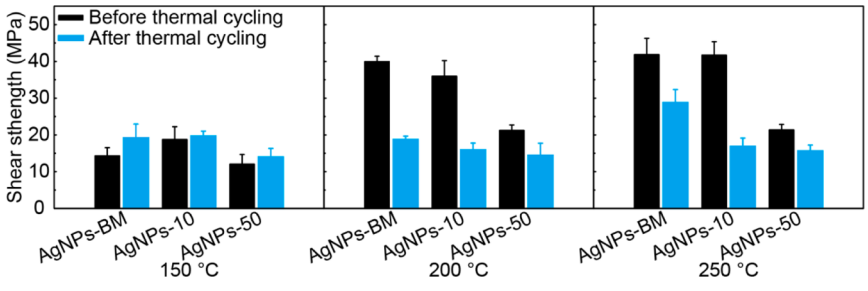

Figure 6. Shear strengths of three types of sandwiched AgNPs samples after initially sintering at 150−250 °C for 30 min and subsequently undergoing thermal cycling from 50 to 200 °C for 1000 cycles.

DOI: 10.1021/acsami.5b01341
ACS Appl. Mater. Interfaces 2015, 7, 9157−9168

produce significant stress on the interconnection interfaces and may worsen the SSs of the sandwiched samples during thermal cycling.[25,27] According to Figure 7, the CTE values for three types of AgNPs-BM (initially sintered at 150, 200, and 250 °C) from 30 to 200 °C are calculated as 2.5×10^{-6}, 7.5×10^{-6}, and 19.4×10^{-6} °C^{1-}, respectively. The CTEs for the former two types of AgNPs-BM are found to be more suitable for the CTE of Si ($3.5-4.5 \times 10^{-6}$ °C^{-1}) or ceramic ($4-8 \times 10^{-6}$ °C^{-1}),[47] which may further reduce the thermo-mechanical stress and improve the interconnection reliability during thermal cycling. However, the reality is that the value of the SS for the latter type of AgNPs-BM (initial sintering at 250 °C) is approximately 10 MPa higher than those for the former two types of AgNPs-BM after thermal cycling (Supporting Information Table S7).

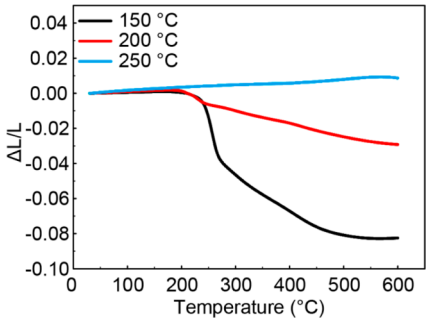

Figure 7. Expansion behaviors of three types of AgNPs-BM (initial sintering at 150, 200, and 250 °C for 30 min) with increasing temperature in the range 30–600 °C.

One probable reason for this phenomenon is that the sintering processes for the former two types of AgNPs-BM are incomplete. As listed in Table 2, the CTEs for the former two types of AgNPs-BM from 200 to 600 °C are -2.10×10^{-4} and -7.61×10^{-5} °C^{-1}, respectively. Distinct shrinkage will inevitably occur as the cycling time is prolonged, producing more thermal mismatches and interfacial stresses in the AgNP interconnection structures. However, the CTE for the latter type of AgNPs-BM from 200 to 600 °C remains stable (13.1×10^{-6} °C^{-1}); therefore, the interfacial stress will at least not increase during long-term thermal cycling. Another plausible explanation involves the existence of the high density twins inside of the sintered structures. It is accepted that the ability of a sintered structure to rapidly deform to failure depends on the ability of its dislocations to move.[48] However, the twin boundary can effectively block the dislocation motion; as a result, the risk of thermal cycling fatigue will decrease as the twin density inside of the sintered structure increases.[49−51] On the basis of Table 1, the value of n at 250 °C is less than that at 150 or 200 °C. Thus, the twin density of the sintered structure for AgNPs-BM at 250 °C is larger than that at the other two temperatures. Therefore, the sandwiched samples of AgNPs-BM after sintering at 250 °C will have better thermal cycling performance and better satisfy the high temperature stability requirement.

Table 2. CETs[a] of Three Types of AgNPs-BM (Initial Sintering at 150, 200, and 250 °C for 30 min), Bulk Ag, Ceramic Substrate, and Si Chip with Increasing Temperature in the Range 30−600 °C

	AgNPs-BM					
	150 °C	200 °C	250 °C	bulk Ag	ceramic substrate	Si chip
30−200 °C	2.5	7.5	19.4	19.5	4−8	3.5−4.5
200−600 °C	−210	−76.1	13.1			

[a]The unit of CET is given in 10^{-6} °C^{1-}.

Sintering Kinetics of AgNPs-BM. On the basis of the above-mentioned study, we confirm that an excellent TIM with high thermal and mechanical performances can be produced using AgNPs-BM. However, some unsolved issues remain, particularly that of the temperature dependence of the sintering process and its effect on the sintering performances. Hence, the sintering kinetics of the AgNPs-BM should be estimated. Figure 8a shows DSC heat flow curves for the three types of the sintered AgNPs from 120 to 260 °C. Two exothermic peaks at approximately 120−180 and 180−230 °C are clearly observed during each sintering process. Because the samples are kept at 120 °C for 20 min, the water in the sintered samples should have evaporated completely, and all heat flow curves show a leveling off between 120 and 130 °C. However, with increasing temperature, the organic layers protecting the AgNPs may not be tightly packed and may even begin to decompose. Because fewer organic molecules are available to hinder the spontaneous coarsening of the AgNPs, the first exothermic peaks are observed. More importantly, the percentage weight losses (particularly in AgNPs-BM and AgNPs-10) start to increase at 130 °C on the basis of the TGA curves in Figure 8b, while the rapid growth of CSs for AgNPs-BM and AgNPs-10 also starts to increase at 130 °C (Figure 4b). Therefore, we doubt that the decomposition of the organic layers and the spontaneous coarsening of AgNPs occur simultaneously in this temperature range. In addition, we also observe that the enthalpy area of the first exothermic peak seems to decrease as the content of the large particles increases (Figure 8a), indicating that the sintered

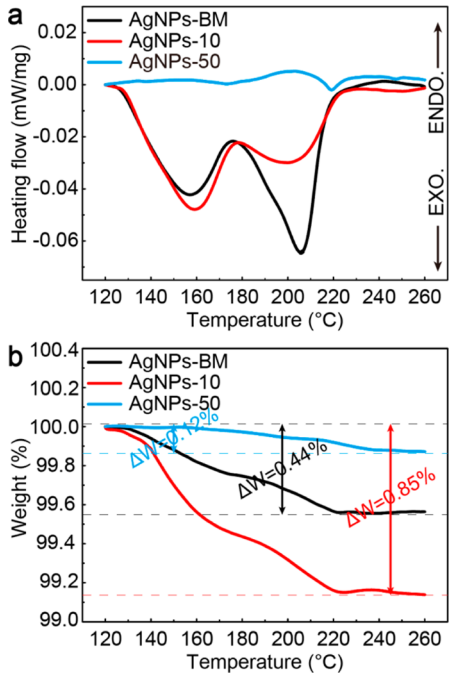

Figure 8. (a) DSC heat flow curves and (b) TGA curves for the three types of AgNPs from 120 to 260 °C.

DOI: 10.1021/acsami.5b01341
ACS Appl. Mater. Interfaces 2015, 7, 9157−9168

process is much more difficult for the larger particles. However, the differences in the enthalpy area of the exothermic peak between AgNPs-BM and AgNPs-10 are not substantial, suggesting that the total driving force for AgNPs-BM during sintering at 120−180 °C does not decrease excessively, even if some large particles are mixed with the small ones.

On the basis of the TGA curves in Figure 8b, the percentage weight losses steadily decrease until 230 °C. Therefore, the endothermic decomposition of the organic layers cannot be responsible for the dramatic upward convex curves at 160−200 °C (Figure 8a). In other words, the existence of the second exothermic peaks at 180−230 °C is more likely associated with another dominant exothermic mechanism rather than the spontaneous coarsening mechanism that produces the first exothermic peaks. Compared to the actual sintered structures at 200−250 °C (Figure 3c,d), the most remarkable phenomena are the complete disappearance of the original ray-like grains from the sintered frames and the rapid decrease in the number of grain boundaries in these frames. Therefore, it is reasonable to assume that the generation of the second exothermic peak might be related to the migration and annihilation of the grain boundaries (or twin boundaries) inside of the frames, and the corresponding enthalpy area should reflect the reduction of the crystallographic defects. Because the enthalpy area of the second exothermic peak for AgNPs-BM is much larger than those of the unimodal AgNPs, its sintered structure would maintain the lowest defect density after 230 °C, consistent with the CS calculations in Figure 4b. In addition, all heat flow curves show horizontal changes at 230−250 °C, indicating that the sintering processes are almost complete after 230 °C.

Sintering Evolution of the Citrates in AgNPs-BM. The sintering process for the AgNP paste consists of two simultaneous evolutions, those of the citrates and AgNPs, which are mutual and associated with each other until the citrates are thoroughly degraded. Figure 9 shows the Raman spectroscopy results for AgNPs-BM sintered at 30−250 °C for 30 min as well as the tentative assignments of a number of citrate bands. For sintering at 30 °C, the principal band is found at 1536 cm^{-1}, followed by bands at 294, 688, 1057, 1328, and 1518 cm^{-1}. On the basis of a previous study, the principal band is assigned to the carboxylate antisymmetric stretching mode (ν_{as}(COO)), and its dominant intensity reflects the interaction between one carboxylate and the Ag surface.[52] The relatively intense bands at 1328 and 1518 cm^{-1} are assigned to the carboxylate symmetric stretching mode (ν_s(COO)) and another ν_{as}(COO) mode,[32,53] and the relatively low intensities of these two bands indicate that they may not bond directly to the Ag surface. Because the difference in frequency between the two ν_{as}(COO) modes is only 18 cm^{-1}, this finding can be best rationalized by the binding of one terminal carboxylate to the Ag surface, while the other terminal carboxylate and the tertiary carboxylate remain unbound. Moreover, the single narrow band at 294 cm^{-1}, assigned to the silver−carboxylate vibration mode (ν(COO−Ag)),[52,54] also confirms that only carboxylate groups bond to the Ag surface. In addition, the existence of another narrow band at 688 cm^{-1}, assigned to the carboxylate deformation (δ(COO)),[32,55] indicates that this silver−carboxylate bonding structure may not be perfectly perpendicular to the Ag surface.

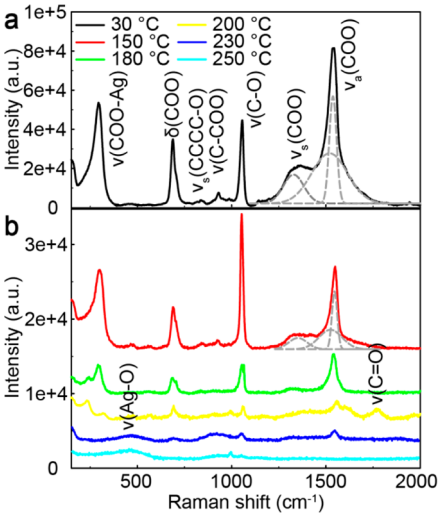

Figure 9. Raman spectra of AgNPs-BM sintered at (a) 30 °C and (b) 150−250 °C for 30 min.

After sintering at 150 °C, no notable changes in frequency are observed for these bands, but the intensities decrease to approximately 15% of their original values (at 30 °C). These decreases in the intensity of the bands accompanied by minor changes in frequency are important signals of significant changes in the microstructure of the AgNPs during sintering, as shown in Figure 3a,b. In addition, we note that the principal band has shifted to 1057 cm^{-1}. This band is assigned to the carbon−oxygen stretch (ν(C—O)) of the tertiary alcohol,[52] and its increasing intensity may indicate that the hydroxyl group also creates a bond with the Ag surface, just as the carboxylate group does. After sintering at 180−200 °C, the intensities of all the strong bands have further decreased, except for a new band generated at 1790 cm^{-1} (yellow line in Figure 9). It is accepted that citric acid will melt at 153 °C and further decompose to form acetoacetic acid at 175 °C. Therefore, this new band, assigned to the carbonyl group (ν(C═O)),[56] should originate from the acetoacetic acid due to citrate decomposition. After sintering at 230−250 °C, all intense bands have almost disappeared, except for another new band at 464 cm^{-1}. This band is assigned to the silver−oxygen vibration mode (ν(Ag—O)),[55] and its formation may be explained by the reoxidation of the freshly reduced Ag during sintering.

Because the citric acid molecule has four functional groups (three carboxyl groups and one hydroxyl group), the nature of the bonding structures between the citrates and Ag surface is quite complicated. In 1995, Munro et al.[52] proposed a monodentate binding mode based on their Raman study, in which two carboxylate groups are bound to the Ag surface while another carboxylate group remains unbound. However, we observed strong intensities of the ν_{as}(COO) and ν(C—O) groups, which were absent in their study (black line in Figure 9), but failed to detect bands reported to be intense in their study (i.e., the carbon−carbon stretching mode (ν(C—COO)) and the three carbon−oxygen symmetric stretching mode (ν_s(CCCO))). Therefore, Munro's model may not fit the bonding structure between the citrates and Ag in our AgNPs-BM paste. In the attempt to develop an appropriate model, the study of the interaction between the ceria NPs and nitrilotriacetic acids provides useful clues. Ahniyaz et al.[57] found that the nitrilotriacetic acids can act as ligands via their carboxylate groups and the lone-pair electrons of nitrogen atoms to connect the cerium ions, where the resultant complexes are better able to stabilize the ceria particles. In this mechanism, the citrate acids can also achieve similar structures, and a potential model

DOI: 10.1021/acsami.5b01341
ACS Appl. Mater. Interfaces 2015, 7, 9157−9168

of the interaction between the citrate and Ag surface is proposed, as shown in Figure 10. Specifically, one of the

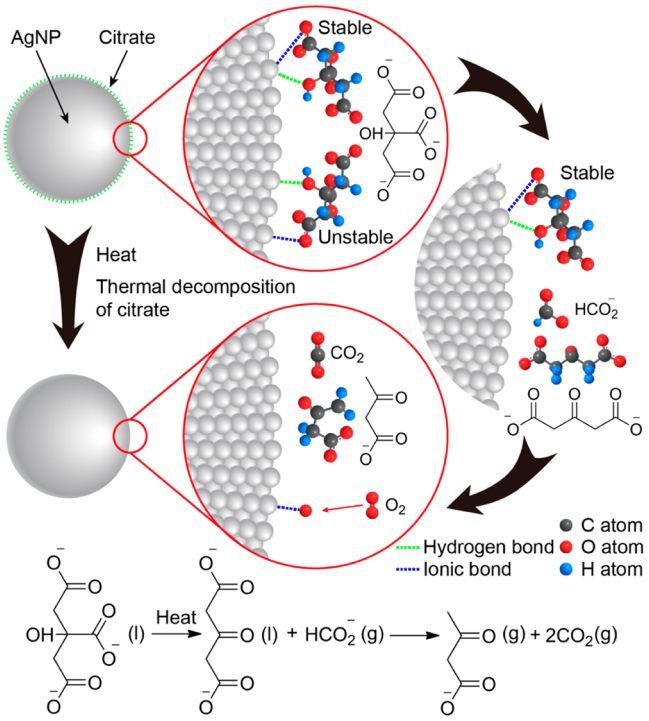

Figure 10. Schematic illustration of the detachment and decomposition of citrates from the surfaces of AgNPs. The decomposition equations for the citrates are also presented.

terminal carboxylate groups and the hydroxyl group are bonded to the Ag surface via ionic and hydrogen bonds, respectively. These two bonds may interact with one Ag atom (the resultant structure would be stable) or two separate Ag atoms (the resultant structure would be unstable). As the sintered temperature increases, certain unstable bonds between the citrates and Ag atoms will break starting at 130 °C, and the generated free citrates may sublimate below 153 °C or volatilize above 153 °C. The decomposition of the citrates will begin at 180 °C (because we observe the ν(C═O) group at 200 °C), initially forming acetonedicarboxylic acid and then spontaneously decarboxylating to generate acetoacetic acid.[52] However, some stable bonds between the citrates and Ag atoms can persist to 230 °C, as the bands of the ν(C—O) group and ν_{as}(COO) group are observed to exist up to this temperature (blue line in Figure 9). In addition, the decomposition products, such as the methanoic acid and carbon dioxide, will volatilize rapidly, and when the citrate acids have completely decomposed after 230 °C, the surface of the AgNPs will be reoxidized by oxygen.

Sintering Evolution of the AgNPs in AgNPs-BM. Interestingly, if we assume that the percentage weight losses of the TGA curves from 120 to 250 °C (Figure 8b) are induced by the complete decomposition of the citrates, the encapsulated densities of citrates on the surfaces of three types of AgNPs can be further established. The calculations are described in the Supporting Information. On the basis of Table 3, the encapsulated densities for AgNPs-BM, AgNPs-10, and AgNPs-50 are 3.36×10^{17}, 4.77×10^{17}, and 3.35×10^{17} m^{-2}, respectively. Therefore, not all surface atoms of AgNPs can connect to the citrates. In other words, the coarsening of the

Table 3. Encapsulated Densities[a] of the Citrates for Three Types of AgNPs

	AgNPs-BM	AgNPs-10	AgNPs-50
encapsulated density	8.41×10^{17}	1.03×10^{18}	6.59×10^{17}

[a]The encapsulated densities are given in m^{-2}.

AgNPs, which consolidates the AgNPs, can occur, although the citrates may not decompose completely.

Tang et al.[58] believed that the major mechanisms of coarsening involve both Ostwald ripening and coalescence. Ostwald ripening occurs by the diffusion of Ag atoms in the organic layers from one AgNP, which then transfer to another. Because the coordination of a surface atom for a small AgNP is lower than that for a large one, the surface atoms for the small particle will be more easily removed. Accordingly, when the Ag in the organic layers is supersaturated, the free Ag atoms will condense on the surfaces of the larger AgNPs. Therefore, the smaller AgNPs shrink, while the larger AgNPs grow.[59,60] In addition, we can imagine that the chemical bonds between the citrates and the Ag surfaces may be weakened or compromised due to the increasing number of the adsorbed Ag atoms, especially when the carboxylate and hydroxyl groups for one citric acid molecule are bonded to different Ag atoms. Another major mechanism is coalescence, which occurs when two AgNPs collide and merge to form a large particle.[58,61] Because the large nanoparticles always have relatively high stability and more energy is required to eliminate the interfaces among them, coalescence is more difficult. However, the small nanoparticles are less stable due to their higher specific surface areas and thus tend to agglomerate during low temperature sintering.

Following the above-mentioned mechanisms, we can reconsider the structural evolution of AgNPs-BM sintered at 150 °C (Figure 3b). There are two special sintered structures inside the sintered islands: large grains, which are 50−80 nm in diameter, and ray-like grains, which are 40−80 nm in height and 5−10 nm in width. The large grains apparently originated from the initial AgNPs-50 via Ostwald ripening. However, the causes of the formation of these ray-like grains remain unknown. Owing to their width bounds, they are more likely related to the original AgNPs-10 via coalescence. To demonstrate this relationship, an in situ TEM observation of the sintering process for several AgNPs-10 was performed at 150 °C (for more details, see the Supporting Information movie). As shown in Figure 11a, seven AgNPs-10, whose (111) planes have been marked by white lines, are observed to have agglomerated with each other at 0 s, but the phase boundaries can be clearly detected, as shown by dashed white lines. However, after sintering for 20 s (Figure 11b), high angle grain boundaries appear to replace the original phase boundaries, and the overlapping regions of AgNPs-10 begin to shrink. After sintering for 40−46 s (Figure 11c−e), numerous coherent twin boundaries are generated and annihilated over time. The formation of these twins is possibly related to the shrinkage or deformation of the sintered AgNPs, as a distinct line-like structure with a width of 11.5 nm is observed after sintering at 150 °C for 49 s (Figure 11f). Noticeably, the line-like structure, created by the coalescence of AgNPs-10, is essentially the same shape as the ray-like grain in the sintered island, and the direction of its long axis is nearly parallel to the $[1\bar{1}1]$ plane of the Ag lattice, which is reported to be the dominant growth orientation of one-dimensional Ag nanostructures.[59,62] Put

DOI: 10.1021/acsami.5b01341
ACS Appl. Mater. Interfaces 2015, 7, 9157−9168

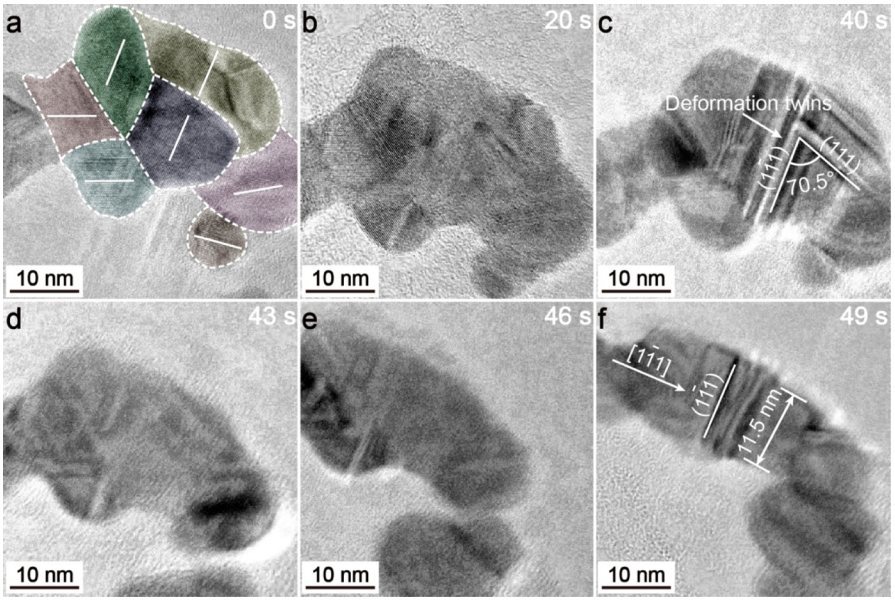

Figure 11. In situ TEM heating images for the formation of a line-like grain by several AgNPs-10 at 150 °C with sintering durations from 0 to 49 s: (a) 0, (b) 20, (c) 40, (d) 43, (e) 46, and (f) 49 s. The AgNPs-10 are delineated by dashed white lines, and the (111) planes of the Ag crystals are indicated by solid white lines.

simply, the ray-like grains should be generated due to the coalescence of AgNPs-10, and our observation has provided definite evidence of the structural evolution of AgNPs-10 in AgNPs-BM paste during sintering at temperatures up to 150 °C.

Another distinguishing feature of the morphological evolution of AgNPs-BM is that the ray-like grains wrapped on the surfaces of the sintered frames gradually disappear with increasing sintering temperature in the range 200−250 °C (Figure 3c−d). Figure 12 shows a locally magnified TEM image

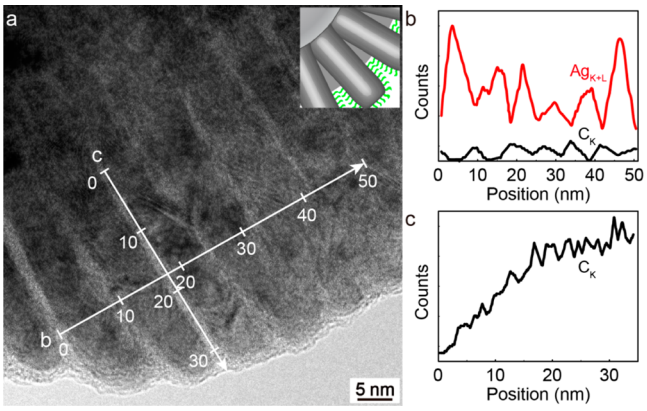

Figure 12. (a) Locally magnified TEM image of a sintered frame for AgNPs-BM after initial sintering at 200 °C for 30 min. (b) Ag and C distributions and (c) C distribution along two perpendicular lines in part a scanned using TEM.

of a sintered frame, with two white lines indicating the measurements of the Ag and carbon (C) distributions. The results demonstrate that each ray-like grain is a single crystal with good Ag crystallization; however, some chaos zones, composed of the residual citrates and amorphous Ag phase, are observed between the adjacent ray-like grains. The C concentration in the chaos zone will decrease rapidly when the measured location is closer to the center of the sintered frame, indicating that the citrates are gradually eliminated or excreted from the chaos zones over time. In addition, organic layers with 2−3 nm in thickness are detected at the tips of the ray-like grains, demonstrating that the citrates can still protect the sintered structure from oxidation before complete decomposition.

The chaos zones among the ray-like grains will eventually disappear from the sintered frames. To better understand this structural evolution, another in situ TEM observation of a typical sintered frame was performed at 250 °C for 1 min. Before sintering, the chaos zones and ray-like grains were arranged alternately by the zigzag boundaries (Figure 13a). The thickness of the chaos zone is in the range 2−5 nm, and each ray-like grain has a long-axis direction of [111] with the [011] direction as the surface normal (Figure 13b). Note that the line-like structure created by the coalescence of the AgNPs-10 also shares the [111] growth orientation, which proves that the ray-like grains indeed originate from the AgNPs-10. In contrast, after sintering at 250 °C for 1 min, the sintered frame exhibits little change in shape but superior crystallization than it had before (Figure 13c). The Ag grains still choose the [011] direction as the surface normal, but the [111], [1$\bar{1}$1], and [200] directions have been rotated 75° clockwise (Figure 13d). Moreover, the original chaos zones have been completely annihilated from the sintered frame, although several {111}/⟨112⟩ type coherent twin boundaries are generated. The twin boundaries are perfectly straight and have an angle of 4° anticlockwise with respect to the original boundaries of the chaos zone. In addition, the twins follow an ATA sequence with twinning elements (e.g., A (1$\bar{1}$1)/[$\bar{1}$12] and T (1$\bar{1}$1)/[1$\bar{1}$2]).

The formation of these coherent twins is undoubtedly related to the crystallization of the chaos zones (the amorphous Ag phase) and the rearrangement of the ray-like grains, and a potential mechanism of twin formation during sintering is thus proposed, as shown in Figure 14. Initially, the ray-like grains are encapsulated by numerous citrates. However, due to the Ostwald ripening of AgNPs, Ag atoms will rapidly diffuse into the citrates. Consequently, the citrates may decompose with

DOI: 10.1021/acsami.5b01341
ACS Appl. Mater. Interfaces 2015, 7, 9157−9168

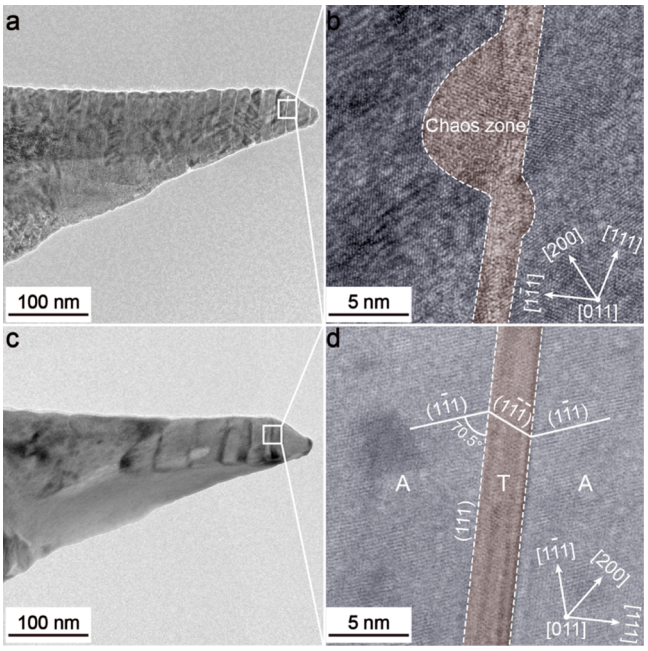

Figure 13. In situ TEM heating images of the formation of the coherent twins in a typical sintered frame at 250 °C for 1 min: (a) low and (b) high magnification TEM images before sintering; (c) low and (d) high magnification TEM images after sintering.

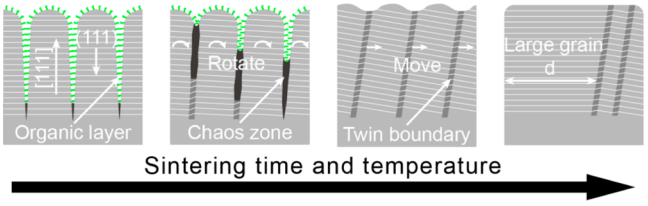

Figure 14. Potential mechanism for twin formation during sintering.

increasing temperature and time, and the diffusing Ag atoms must separate from the organic layers and may crystallize to form the amorphous Ag phase. Because the citrates are always eliminated from the roots of the chaos zones, the crystallization of the amorphous Ag phase in these zones may first occur at the roots of the ray-like grains and then spread toward the tips of the chaos zones. As a result, one ray-like grain will rotate to its adjacent grains, and the generated crystallization stress can cause the coherent twins to bond to the adjacent grains with similar orientations. In addition, the generated twin boundaries may move or be eliminated from the free surfaces during sintering; thus, the number of the coherent twins is less than that in the chaos zones (Figure 13a,c). On the basis of the above-mentioned analysis, we can confirm that the high density twins inside of the sintered structure are generated by the stress-induced crystallization of the chaos zones, and the density of these twins will increase with the formation of the chaos zones but decrease after these zones have completely disappeared.

Finally, we can summarize the structural evolution of AgNPs in AgNP-BM paste during sintering. Initially (Figure 15a), AgNPs-10 are packed around AgNPs-50 without uncontrolled agglomeration. As the temperature increased in the range 120–180 °C (Figure 15b), the AgNPs experience spontaneous sintering triggered by the desorption of citrates from their surfaces. In particular, AgNPs-50 grow larger via Ostwald

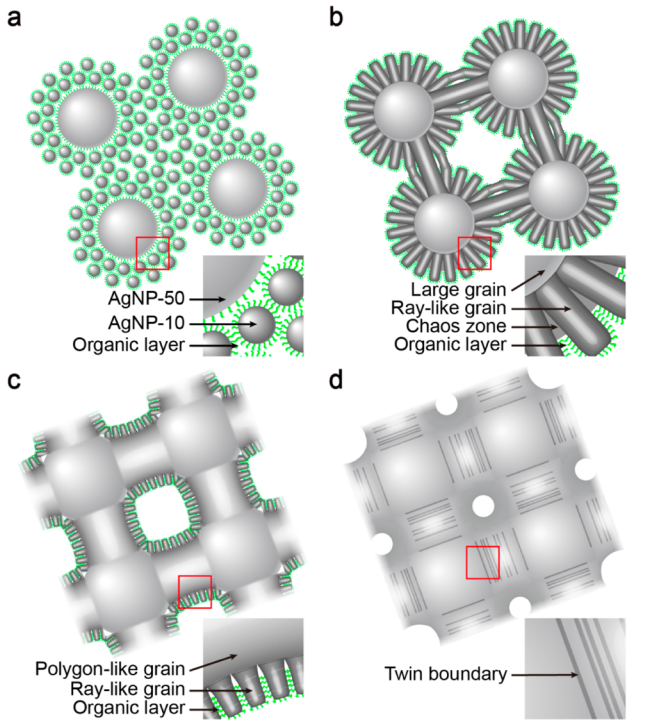

Figure 15. Sintering evolution model of AgNPs in AgNP-BM paste: (a) before sintering, (b) after sintering at 120–180 °C, (c) after sintering at 180–230 °C, (d) after sintering at 230–250 °C.

ripening, while AgNPs-10 transfer to the ray-like grains via coalescence; the resultant structures cluster together to form sintered islands. As the temperature increases in the range 180–230 °C (Figure 15c), the sintered islands will transform into the sintered frames, which can further thicken via the rearrangement of the ray-like grains and the crystallization of the chaos zones. In addition, coherent twins will also be generated in these sintered frames via the structural evolution of the ray-like grains and the chaos zones. As the temperature increases in the range 230–250 °C (Figure 15d), the ray-like grains are completely consumed, and the sintered frames transfer to the three-dimensional network with the high density coherent twins inside; this structural evolution makes the sintered structure more compact and leads to an ultrahigh thermal conductivity, reaching 65% that of bulk Ag, as well as high structural stability during high temperature usage.

CONCLUSIONS

In conclusion, a bimodal AgNP paste with ultrahigh thermal conductivity and structural stability has been synthesized by the simple ultrasonic mixing of two types of unimodal AgNPs. After sintering at 250 °C for 30 min, the thermal conductivity of this paste can reach 278.5 W m^{-1} K^{-1}, close to 65% of the theoretical value of the bulk Ag. The shear strength can approach 28.75 MPa after thermal cycling for 1000 cycles, which is far higher than the values obtained for Sn-based solders in similar conditions. Moreover, on the basis of the calculation of the exponent of TC (n), we confirm that a high density of coherent twins has formed inside of the sintered structures of AgNP-BM. Due to the low scattering effect and effective blockage of the dislocation motion of the coherent twin boundaries, a sintered structure of AgNP-BM has been achieved with high thermal conductivity and without reduction of the shear strength during thermal cycling. In addition, the

DOI: 10.1021/acsami.5b01341
ACS Appl. Mater. Interfaces 2015, 7, 9157–9168

sintering behaviors of AgNP-BM, including the citrates and AgNPs, are discussed in detail. On the basis of our Raman study, we propose a potential interaction model between citrate and Ag in which one of the terminal carboxylate groups and the hydroxyl group of the citrate are bonded to the Ag surface via ionic and hydrogen bonds, respectively. As revealed by two in situ TEM observations, both types of AgNPs in the AgNP-BM paste would experience spontaneous sintering, and the AgNPs-50 will grow larger via Ostwald ripening, while AgNPs-10 will transfer to the ray-like grains via coalescence. The ray-like grains will gradually rotate due to the crystallization of the chaos zones, and these chaos zones will further transfer to form the coherent twins; the final sintered structure will be more compact and solid, leading to high thermal conductivity and shear strength. Therefore, we believe that this bimodal AgNP paste has great potential as an excellent thermal interface material for high temperature power device applications.

■ ASSOCIATED CONTENT

Supporting Information

Optimization of the weight ratio for the bimodal AgNP paste, crystallite size calculations for three types of AgNPs, thicknesses of the organic protecting layers for AgNPs-10 and AgNPs-50, thermal conductivity calculations for three types of AgNPs, encapsulated density calculations for three types of AgNPs, and the movie of the in situ TEM observation of AgNPs-10. The Supporting Information is available free of charge on the ACS Publications website at DOI: 10.1021/acsami.5b01341.

■ AUTHOR INFORMATION

Corresponding Authors

*E-mail: myli@hit.edu.cn.
*E-mail: zhzhang@hitsz.edu.cn.

Notes

The authors declare no competing financial interest.

■ ACKNOWLEDGMENTS

The authors gratefully acknowledge the financial support of the National Natural Science Foundation of China under Grant 51305103, Shenzhen Science and Technology Plan Project under Grant XCL201110007, and China Postdoctoral Science Foundation under Grant 2013M530153.

■ REFERENCES

(1) Bastús, N. G.; Merkoçi, F.; Piella, J.; Puntes, V. Synthesis of Highly Monodisperse Citrate-Stabilized Silver Nanoparticles of up to 200 nm: Kinetic Control and Catalytic Properties. *Chem. Mater.* **2014**, *26*, 2836−2846.
(2) Wodka, D.; Bielanska, E.; Socha, R. P.; Elzbieciak-Wodka, M.; Gurgul, J.; Nowak, P.; Warszyński, P.; Kumakiri, I. Photocatalytic Activity of Titanium Dioxide Modified by Silver Nanoparticles. *ACS Appl. Mater. Interfaces* **2010**, *2*, 1945−1953.
(3) Yan, Z. J.; Shah, R. A.; Chado, G.; Gray, S. K.; Pelton, M.; Scherer, N. F. Guiding Spatial Arrangements of Silver Nanoparticles by Optical Binding Interactions in Shaped Light Fields. *ACS Nano* **2013**, *7*, 1790−1802.
(4) AshaRani, P. V.; Low Kah Mun, G. L. K.; Hande, M. P.; Valiyaveettil, S. Cytotoxicity and Genotoxicity of Silver Nanoparticles in Human Cells. *ACS Nano* **2008**, *3*, 279−290.
(5) Nallathamby, P. D.; Xu, X. H. N. Study of Cytotoxic and Therapeutic Effects of Stable and Purified Silver Nanoparticles on Tumor Cells. *Nanoscale* **2010**, *2*, 942−952.
(6) Asoro, M. A.; Kovar, D.; Ferreira, P. J. Effect of Surface Carbon Coating on Sintering of Silver Nanoparticles: In Situ Tem Observations. *Chem. Commun.* **2014**, *50*, 4835−4838.
(7) Asare, N.; Instanes, C.; Sandberg, W. J.; Refsnes, M.; Schwarze, P.; Kruszewski, M.; Brunborg, G. Cytotoxic and Genotoxic Effects of Silver Nanoparticles in Testicular Cells. *Toxicology* **2012**, *291*, 65−72.
(8) Magdassi, S.; Grouchko, M.; Berezin, O.; Kamyshny, A. Triggering the Sintering of Silver Nanoparticles at Room Temperature. *ACS Nano* **2010**, *4*, 1943−1948.
(9) Hu, A.; Guo, J. Y.; Alarifi, H.; Patane, G.; Zhou, Y.; Compagnini, G.; Xu, C. X. Low Temperature Sintering of Ag Nanoparticles for Flexible Electronics Packaging. *Appl. Phys. Lett.* **2010**, *97*, 153117.
(10) Yan, J. F.; Zou, G. S.; Wu, A. P.; Ren, J. L.; Yan, J. C.; Hu, A. M.; Zhou, Y. Pressureless Bonding Process Using Ag Nanoparticle Paste for Flexible Electronics Packaging. *Scr. Mater.* **2012**, *66*, 582−585.
(11) Maruyama, M.; Matsubayashi, R.; Iwakuro, H.; Isoda, S.; Komatsu, T. Silver Nanosintering: A Lead-Free Alternative to Soldering. *Appl. Phys. A: Mater. Sci. Process.* **2008**, *93*, 467−470.
(12) Yu, H.; Li, L. L.; Zhang, Y. J. Silver Nanoparticle-Based Thermal Interface Materials with Ultra-Low Thermal Resistance for Power Electronics Applications. *Scr. Mater.* **2012**, *66*, 931−934.
(13) Alayli, N.; Schoenstein, F.; Girard, A.; Tan, K. L.; Dahoo, P. R. Spark Plasma Sintering Constrained Process Parameters of Sintered Silver Paste for Connection in Power Electronic Modules: Microstructure, Mechanical and Thermal Properties. *Mater. Chem. Phys.* **2014**, *148*, 125−133.
(14) Shahil, K. M. F.; Balandin, A. A. Graphene−Multilayer Graphene Nanocomposites as Highly Efficient Thermal Interface Materials. *Nano Lett.* **2012**, *12*, 861−867.
(15) Liang, Q. Z.; Yao, X. X.; Wang, W.; Liu, Y.; Wong, C. P. A Three-Dimensional Vertically Aligned Functionalized Multilayer Graphene Architecture: An Approach for Graphene-Based Thermal Interfacial Materials. *ACS Nano* **2011**, *5*, 2392−2401.
(16) Steinigeweg, D.; Schlucker, S. Monodispersity and Size Control in the Synthesis of 20−100 nm Quasi-Spherical Silver Nanoparticles by Citrate and Ascorbic Acid Reduction in Glycerol-Water Mixtures. *Chem. Commun.* **2012**, *48*, 8682−8684.
(17) Dong, X. Y.; Ji, X. H.; Wu, H. L.; Zhao, L. L.; Li, J.; Yang, W. S. Shape Control of Silver Nanoparticles by Stepwise Citrate Reduction. *J. Phys. Chem. C* **2009**, *113*, 6573−6576.
(18) Tung, H. T.; Chen, I. G.; Kempson, I. M.; Song, J. M.; Liu, Y. F.; Chen, P. W.; Hwang, W. S.; Hwu, Y. Shape-Controlled Synthesis of Silver Nanocrystals by X-Ray Irradiation for Inkjet Printing. *ACS Appl. Mater. Interfaces* **2012**, *4*, 5930−5935.
(19) Zhang, R. W.; Moon, K. S.; Lin, W.; Wong, C. P. Preparation of Highly Conductive Polymer Nanocomposites by Low Temperature Sintering of Silver Nanoparticles. *J. Mater. Chem.* **2010**, *20*, 2018−2023.
(20) Wang, S.; Li, M. Y.; Ji, H. J.; Wang, C. Q. Rapid Pressureless Low-Temperature Sintering of Ag Nanoparticles for High-Power Density Electronic Packaging. *Scr. Mater.* **2013**, *69*, 789−792.
(21) Nam, S.; Cho, H. W.; Kim, T.; Kim, D.; Sung, B. J.; Lim, S.; Kim, H. Effects of Silica Particles on the Electrical Percolation Threshold and Thermomechanical Properties of Epoxy/Silver Nanocomposites. *Appl. Phys. Lett.* **2011**, *99*, 043104.
(22) Khazaka, R.; Mendizabal, L.; Henry, D. Review on Joint Shear Strength of Nano-Silver Paste and Its Long-Term High Temperature Reliability. *J. Electron. Mater.* **2014**, *43*, 2459−2466.
(23) Wang, T.; Chen, X.; Lu, G. Q.; Lei, G. Y. Low-Temperature Sintering with Nano-Silver Paste in Die-Attached Interconnection. *J. Electron. Mater.* **2007**, *36*, 1333−1340.
(24) Moon, K. S.; Dong, H.; Maric, R.; Pothukuchi, S.; Hunt, A.; Li, Y.; Wong, C. P. Thermal Behavior of Silver Nanoparticles for Low-Temperature Interconnect Applications. *J. Electron. Mater.* **2005**, *34*, 168−175.
(25) Wang, T.; Chen, G.; Wang, Y. P.; Chen, X.; Lu, G. Q. Uniaxial Ratcheting and Fatigue Behaviors of Low-Temperature Sintered Nano-Scale Silver Paste at Room and High Temperatures. *Mater. Sci. Eng., A* **2010**, *527*, 6714−6722.

DOI: 10.1021/acsami.5b01341
ACS Appl. Mater. Interfaces 2015, 7, 9157−9168

(26) Siow, K. S. Mechanical Properties of Nano-Silver Joints as Die Attach Materials. *J. Alloys Compd.* **2012**, *514*, 6−19.
(27) Heuck, N.; Palm, G.; Sauerberg, T.; Stranz, A.; Waag, A.; Bakin, A. SiC-Die-Attachment for High Temperature Applications. *Mater. Sci. Forum* **2010**, *645*−*648*, 741−744.
(28) Chun, K. Y.; Oh, Y.; Rho, J.; Ahn, J. H.; Kim, Y. J.; Choi, H. R.; Baik, S. Highly Conductive, Printable and Stretchable Composite Films of Carbon Nanotubes and Silver. *Nat. Nanotechnol.* **2010**, *5*, 853−857.
(29) Zhang, R. W.; Moon, K. S.; Lin, W.; Wong, C. P. Preparation of Highly Conductive Polymer Nanocomposites by Low Temperature Sintering of Silver Nanoparticles. *J. Mater. Chem.* **2010**, *20*, 2018−2023.
(30) Frens, G.; Overbeek, J. T. G. Carey Lea's Colloidal Silver. *Kolloid Z. Z. Polym.* **1969**, *233*, 922−929.
(31) Lee, P. C.; Meisel, D. Adsorption and Surface-Enhanced Raman of Dyes on Silver and Gold Sols. *J. Phys. Chem.* **1982**, *86*, 3391−3395.
(32) Siiman, O.; Bumm, L. A.; Callaghan, R.; Blatchford, C. G.; Kerker, M. Surface-Enhanced Raman Scattering by Citrate on Colloidal Silver. *J. Phys. Chem.* **1983**, *87*, 1014−1023.
(33) Exner, H. E.; Petzow, G.; Wellner, P. Problems in the Extension of Sintering Theories to Real Systems. In *Sintering and Related Phenomena*, Kuczynski, G. C., Ed. Springer: New York, 1973; Chapter 30, pp 351−362.
(34) Wonisch, A.; Kraft, T.; Moseler, M.; Riedel, H. Effect of Different Particle Size Distributions on Solid-State Sintering: A Microscopic Simulation Approach. *J. Am. Ceram. Soc.* **2009**, *92*, 1428−1434.
(35) Alvarez, F. X.; Jou, D.; Sellitto, A. Pore-Size Dependence of the Thermal Conductivity of Porous Silicon: A Phonon Hydrodynamic Approach. *Appl. Phys. Lett.* **2010**, *97*, 033103.
(36) Cernuschi, F.; Ahmaniemi, S.; Vuoristo, P.; Mäntylä, T. Modelling of Thermal Conductivity of Porous Materials: Application to Thick Thermal Barrier Coatings. *J. Am. Ceram. Soc.* **2004**, *24*, 2657−2667.
(37) Aivazov, M. I.; Domashnev, I. A. Influence of Porosity on the Conductivity of Hot-Pressed Titanium-Nitride Specimens. *Powder Metall. Met. Ceram.* **1968**, *7*, 708−710.
(38) Desai, T. G. Thermal Transport in Nanoclusters. *Appl. Phys. Lett.* **2011**, *98*, 193107.
(39) Qin, X. Y.; Zhang, W.; Zhang, L. D.; Jiang, L. D.; Liu, X. J.; Jin, D. Low-Temperature Resistance and Its Temperature Dependence in Nanostructured Silver. *Phys. Rev. B: Condens. Matter Mater. Phys.* **1997**, *56*, 10596−10604.
(40) Francl, J.; Kingery, W. D. Thermal Conductivity: IX, Experimental Investigation of Effect of Porosity on Thermal Conductivity. *J. Am. Ceram. Soc.* **1954**, *37*, 99−107.
(41) Thewsey, D. J.; Zhao, Y. Y. Thermal Conductivity of Porous Copper Manufactured by the Lost Carbonate Sintering Process. *Phys. Status Solidi A* **2008**, *205*, 1126−1131.
(42) Wang, Z. J.; Alaniz, J. E.; Jang, W. Y.; Garay, J. E.; Dames, C. Thermal Conductivity of Nanocrystalline Silicon: Importance of Grain Size and Frequency-Dependent Mean Free Paths. *Nano Lett.* **2011**, *11*, 2206−2213.
(43) Lu, L.; Shen, Y. F.; Chen, X. H.; Qian, L. H.; Lu, K. Ultrahigh Strength and High Electrical Conductivity in Copper. *Science* **2004**, *304*, 422−426.
(44) Chen, K. C.; Wu, W. W.; Liao, C. N.; Chen, L. J.; Tu, K. Observation of Atomic Diffusion at Twin-Modified Grain Boundaries in Copper. *Science* **2008**, *321*, 1066−1069.
(45) Han, Y. D.; Jing, H. Y.; Nai, S. M. L.; Xu, L. Y.; Tan, C. M.; Wei, J. Interfacial Reaction and Shear Strength of Ni-Coated Carbon Nanotubes Reinforced Sn−Ag−Cu Solder Joints During Thermal Cycling. *Intermetallics* **2012**, *31*, 72−78.
(46) Šebo, P.; Švec, P.; Janičkovič, D.; Štefánik, P. Influence of Thermal Cycling on Shear Strength of Cu-Sn3. 5AgIn-Cu Joints with Various Content of Indium. *J. Alloys Compd.* **2008**, *463*, 168−172.
(47) Lee, K. N.; Fox, D. S.; Bansal, N. P. Rare Earth Silicate Environmental Barrier Coatings for SiC/SiC Composites and Si_3N_4 Ceramics. *J. Eur. Ceram. Soc.* **2005**, *25*, 1705−1715.
(48) Ovid'ko, I. A.; Sheinerman, A. G. Triple Junction Nanocracks in Deformed Nanocrystalline Materials. *Acta Mater.* **2004**, *52*, 1201−1209.
(49) Lu, K.; Lu, L.; Suresh, S. Strengthening Materials by Engineering Coherent Internal Boundaries at the Nanoscale. *Science* **2009**, *324*, 349−352.
(50) Shen, Y. F.; Lu, L.; Lu, Q. H.; Jin, Z. H.; Lu, K. Tensile Properties of Copper with Nano-Scale Twins. *Scr. Mater.* **2005**, *52*, 989−994.
(51) Yu, Q.; Qi, L.; Chen, K.; Mishra, R. K.; Li, J.; Minor, A. M. The Nanostructured Origin of Deformation Twinning. *Nano Lett.* **2012**, *12*, 887−892.
(52) Munro, C. H.; Smith, W. E.; Garner, M.; Clarkson, J.; White, P. C. Characterization of the Surface of a Citrate-Reduced Colloid Optimized for Use as a Substrate for Surface-Enhanced Resonance Raman Scattering. *Langmuir* **1995**, *11*, 3712−3720.
(53) Marsich, L.; Bonifacio, A.; Mandal, S.; Krol, S.; Beleites, C.; Sergo, V. Poly-L-lysine-Coated Silver Nanoparticles as Positively Charged Substrates for Surface-Enhanced Raman Scattering. *Langmuir* **2012**, *28*, 13166−13171.
(54) Grouchko, M.; Kamyshny, A.; Mihailescu, C. F.; Anghel, D. F.; Magdassi, S. Conductive Inks with a "Built-In" Mechanism That Enables Sintering at Room Temperature. *ACS Nano* **2011**, *5*, 3354−3359.
(55) Tada, H.; Bronkema, J.; Bell, A. T. Application of In Situ Surface-Enhanced Raman Spectroscopy (SERS) to the Study of Citrate Oxidation on Silica-Supported Silver Nanoparticles. *Catal. Lett.* **2004**, *92*, 93−99.
(56) Canamares, M. V.; Garcia-Ramos, J. V.; Gomez-Varga, J. D.; Domingo, C.; Sanchez-Cortes, S. Comparative Study of the Morphology, Aggregation, Adherence to Glass, and Surface-Enhanced Raman Scattering Activity of Silver Nanoparticles Prepared by Chemical Reduction of Ag^+ Using Citrate and Hydroxylamine. *Langmuir* **2005**, *21*, 8546−8553.
(57) Salazar-Sandoval, E. J.; Johansson, M. K. G.; Ahniyaz, A. Aminopolycarboxylic Acids as a Versatile Tool to Stabilize Ceria Nanoparticles−a Fundamental Model Experimentally Demonstrated. *RSC Adv.* **2014**, *4*, 9048−9055.
(58) Tang, Y.; He, W.; Wang, S. X.; Tao, Z. H.; Cheng, L. J. New Insight into the Size-Controlled Synthesis of Silver Nanoparticles and Its Superiority in Room Temperature Sintering. *CrystEngComm* **2014**, *16*, 4431−4440.
(59) Sun, Y. G.; Mayers, B.; Herricks, T.; Xia, Y. N. Polyol Synthesis of Uniform Silver Nanowires: A Plausible Growth Mechanism and the Supporting Evidence. *Nano Lett.* **2003**, *3*, 955−960.
(60) Hui, K. S.; Hui, K. N.; Dinh, D. A.; Tsang, C. H.; Cho, Y. R.; Zhou, W.; Hong, X. T.; Chun, H. H. Green Synthesis of Dimension-Controlled Silver Nanoparticle−Graphene Oxide with In Situ Ultrasonication. *Acta Mater.* **2014**, *64*, 326−332.
(61) Grouchko, M.; Popov, I.; Uvarov, V.; Magdassi, S.; Kamyshny, A. Coalescence of Silver Nanoparticles at Room Temperature: Unusual Crystal Structure Transformation and Dendrite Formation Induced by Self-Assembly. *Langmuir* **2009**, *25*, 2501−2503.
(62) Murph, S. E. H.; Murphy, C. J.; Leach, A.; Gall, K. A Possible Oriented Attachment Growth Mechanism for Silver Nanowire Formation. *Cryst. Growth Des.* **2015**, *15*, 1968−1974.

DOI: 10.1021/acsami.5b01341
ACS Appl. Mater. Interfaces 2015, 7, 9157−9168